

1 **Quantifying the spatial-seasonal patterns of land-atmosphere water, heat and**
2 **CO₂ flux exchange over the Tibetan Plateau from an observational perspective**

3 Binbin Wang^{1,2,5,6,7}, Yaoming Ma^{1,2,3,4,5,6,7*}, Zeyong Hu⁸, Xuan Li¹, Weiqiang Ma^{1,2,}
4 ^{4,5,6,7}, Xuelong Chen^{1,2,5,6,7}, Cunbo Han^{1,2,5,6,7}, Zhipeng Xie^{1,2,5,6,7}, Yuyang Wang⁹,
5 Maoshan Li¹⁰, Bin Ma^{1,5,6,7}, Xingdong Shi^{1,4,7}, Weimo Li^{1,4}, Zhengling Cai^{1,4}

6 ¹State Key Laboratory of Tibetan Plateau Earth System, Resources and Environment (TPESRE),
7 Institute of Tibetan Plateau Research, Chinese Academy of Sciences, Beijing 100101, China;

8 ²College of Earth and Planetary Sciences, University of Chinese Academy of Sciences, Beijing
9 100049, China;

10 ³College of Hydraulic & Environmental Engineering, China Three Gorges University, Yichang
11 443002, China;

12 ⁴College of Atmospheric Science, Lanzhou University, Lanzhou 730000, China;

13 ⁵National Observation and Research Station for Qomolangma Special Atmospheric Processes and
14 Environmental Changes, Dingri 858200, China;

15 ⁶Kathmandu Center of Research and Education, Chinese Academy of Sciences, Beijing 100101,
16 China;

17 ⁷China-Pakistan Joint Research Center on Earth Sciences, Chinese Academy of Sciences, Islamabad
18 45320, Pakistan;

19 ⁸Key Laboratory of Land Surface Process and Climate Change in Cold and Arid Regions, Northwest
20 Institute of Eco-Environment and Resources, Chinese Academy of Sciences, Lanzhou, 730000,
21 China;

22 ⁹College of Grassland Science and Technology, China Agricultural University, Beijing,
23 100193,China;

24 ¹⁰School of Atmospheric Sciences, Chengdu University of Information Technology, Chengdu
25 610225, China

26 Corresponding authors: Binbin Wang (wangbinbin@@itpcas.ac.cn); Yaoming Ma
27 (ymma@itpcas.ac.cn); Address: Building 3, Courtyard 16, Liucui Road, Chaoyang District, Beijing City,
28 China. Zip code: 100101.

36 **Abstract**

37 Land-atmosphere (LA) interactions, through the turbulent exchange of water, heat and CO₂ fluxes,
38 strongly influence regional micro-climates, water cycles, energy budgets, and ecosystem dynamics. The
39 Tibetan Plateau (TP), characterized by its vast extent, high elevation, strong solar radiation and extreme
40 weather variability, remains underexplored due to the scarcity of LA observation sites, particularly in its
41 western and northern regions. This study introduces a newly established research and observation
42 platform, comprising 16 planetary boundary layer towers that span diverse landscapes and dynamic
43 meteorological conditions. Across these sites, mean annual air temperature, wind speed, and liquid
44 precipitation range from -3.5 to 18.5°C, 0.6 to 5.6 m s⁻¹, and 43 to 2164 mm, respectively. Elevation
45 exhibits significant correlations with all meteorological variables, highlighting the pronounced spatial
46 heterogeneity of land-atmosphere coupling across the region. The turbulent fluxes of water and heat
47 exhibit distinct seasonal patterns, with maximum sensible heat flux (*SH*) in April-May and latent heat
48 flux (*LE*) in July-August. Most stations act as carbon sinks, with net ecosystem exchange (*NEE*; the net
49 CO₂ exchange between the ecosystem and the atmosphere, where negative values indicate net ecosystem
50 CO₂ uptake) ranging from -3.2 to -174.3 g C m⁻² a⁻¹, except the Medog station, which behaves as a carbon
51 source likely linked to vegetation disturbance and human activity. *LE* is significantly correlated with *SH*,
52 *NEE* and ecosystem respiration, revealing a strong coupling among water, heat and carbon fluxes. This
53 high-resolution, quality-controlled dataset provides critical in situ observations for studying water-heat-
54 carbon coupling, validating models and satellite algorithms, and improving understanding of climate-
55 ecosystem interactions over the TP. The whole datasets are freely available at the National Tibetan
56 Plateau Data Center (<https://doi.org/10.11888/Atmos.tpd.c.302428>).

57 **Key words:** Land-atmosphere turbulent fluxes, spatial-temporal variations, comprehensive
58 observation and research platform, Tibetan Plateau

59
60
61
62
63
64
65
66
67
68
69
70
71
72
73
74
75
76

77 1 Introduction

78 Land-atmosphere (LA) interactions, which govern the flux exchanges of energy, water, and CO₂
79 between the Earth's surface and the atmosphere, are pivotal in shaping regional water cycles, climate
80 dynamics, and ecosystem changes [Gentine et al., 2019; Ma et al., 2023; Santanello et al., 2018; Seo
81 and Ha, 2022; Zhang et al., 2024]. Thermal contrasts between distinct landforms—such as land vs. water,
82 mountain vs. valley, and ocean vs. land — drive regional circulations like lake-land and mountain-valley
83 breezes, as well as large-scale atmospheric motions, including monsoons [Gerken et al., 2014; Wu and
84 Zhang, 1998; Wu et al., 2023]. These LA interactions modulate a wide range of processes, including the
85 dispersion of air pollutants, the transport of atmospheric moisture, the redistribution of clouds and
86 precipitation, and the regulation of ecosystem carbon balance [Bei et al., 2018; Friedlingstein et al., 2022;
87 Suni et al., 2015; Zhu et al., 2017]. For instance, enhanced coupling between soil moisture and land
88 surface temperature can intensify droughts and heatwaves in northern East Asia [Seo and Ha, 2022],
89 where soil moisture deficits reduce evapotranspiration (ET), amplifying heatwave conditions,
90 particularly in areas with sparse vegetation. Nonlinear feedbacks between ET and cloud formation remain
91 poorly constrained in transitional zones between energy- and water-limited regimes [Zhang et al. 2024].
92 Under global warming, LA interactions governing permafrost thaw, vegetation productivity, and
93 ecosystem respiration play an increasingly important role in determining regional and global carbon
94 budgets, especially over the data scarce regions [Turetsky et al., 2020; Wang et al., 2023b; Wei et al.,
95 2021]. Quantifying these coupled fluxes through in situ observations is thus essential for understanding
96 Earth system responses to climate change.

97 Understanding LA interactions through coordinated, multidisciplinary, and multi-scale observations
98 is crucial for addressing global challenges such as water resource management, land-use planning,
99 climate change, and ecosystem preservation. In this context, key global initiatives—such as the First
100 International Satellite Land Surface Climatology Project Field Experiment (United States) [Sellers et al.,
101 1992], the Hydrologic Atmospheric Pilot Experiment (France, Niger) [André et al., 1986; Goutorbe et
102 al., 1997], the Northern Hemisphere Climate Processes Land Surface Experiment (Sweden) [Halldin et
103 al., 1999], the Boreal Ecosystem–Atmosphere Study (Canada) [Sellers et al., 1995], the Inner Mongolia
104 Semiarid Grassland Soil–Vegetation–Atmosphere Interaction and the Heihe River Basin Field
105 Experiment (China) [Liu et al., 2018; Lü et al., 1997]—have provided foundational insights into LA
106 interactions and have advanced parameterizations for climate models. Tibetan Plateau (TP), one of the
107 world's most climate-sensitive and data-scarce region, plays a particularly critical role in the climate and
108 ecology dynamics. TP exerts remarkable influence on atmospheric processes, generating thermal
109 disturbances that affect circulation patterns, weather, and climate not only in China and East Asia but
110 also globally [Wu and Zhang, 1998; Ye and Wu, 1998]. For example, mesoscale system vortices and shear
111 lines created in the TP's atmospheric boundary layer can lead to extreme weather events, such as heavy
112 rain and storms, impacting both the plateau and surrounding regions [Li et al., 2020; Xu and Chen, 2006].
113 Thus, LA coupling and dynamics are important for the formation and development of weather systems.
114 Over the past few decades, large-scale field activities and long-term observational experiments—such as
115 Qinghai-Xizang Plateau Meteorology Experiment (QXPME), the Tibetan Plateau Atmospheric
116 Scientific Experiment II and III (TIPEX-II, TIPEX-III), the Sino Japanese inter governmental cooperation
117 project (JICA), the Global Energy and Water Cycle Experiment Asian Monsoon Experiment on the
118 Tibetan Plateau (GAME/Tibet), the Coordinated Enhanced Observing Period (CEOP) Asia-Australia
119 Monsoon Project on the Tibetan Plateau (CAMP/Tibet), etc. —have greatly enhanced our understanding

120 of land surface processes in the TP [Huang et al., 2023; Ma et al., 2023], and these efforts have also
121 helped refine climate model parameterization, improving our ability to predict TP's climatic effects.
122 However, the stations for measuring heat, water and CO₂ fluxes are concentrated mostly in the east and
123 still rarely distributed over the vast northern and western regions, hindering our understanding on its
124 spatial distribution and total amounts of heat, water and CO₂ flux. Given the growing challenges posed
125 by global climate change, accurately measuring and modeling LA interaction processes is more critical
126 than ever, and such efforts are essential for predicting climate extremes, managing water resources, and
127 supporting sustainable ecology [Sun et al., 2015].

128 Although several LA interaction studies have analyzed seasonal variations in turbulent fluxes and
129 their controlling factors [Ma et al., 2005; Ma et al., 2018; Ma et al., 2023; Wang et al., 2011; Yang et al.,
130 2008], the lack of spatially distributed eddy-covariance (EC) sites has resulted in large uncertainties in
131 flux estimates and interannual variability, especially over underrepresented ecosystem types over the
132 western and northern TP. Previous modeling and remote-sensing efforts have improved regional *ET*
133 estimates, yet still rely on limited ground validation measurements [Ma and Zhang, 2022; Yuan et al.,
134 2024]. For example, the water-carbon coupled biophysical model [Ma and Zhang, 2022] and an improved
135 *ET* model [Yuan et al., 2021] are validated with EC measurements, both yielding annual *ET* value of
136 approximately 350 mm yr⁻¹. However, factors influencing the inter-annual variations in *ET* exhibit large
137 biases and uncertainties, especially for data-scarce western and northern regions. As for carbon function,
138 TP contains extensive permafrost and a variety of landscapes, including alpine meadows, alpine steppes,
139 alpine shrubs, alpine wetlands, forests, and alpine deserts, which have a substantial impact on the carbon
140 sink/source function of the region, and shows important ecological and environmental consequences.
141 Recent studies indicate that most alpine meadows on the TP function as carbon sinks, with values ranging
142 from -430 to -12.5 g C m⁻² a⁻¹, and some alpine steppe areas act as weak carbon sources [Wang et al.,
143 2023a; Wei et al., 2021]. Specifically, alpine grasslands exhibit a weaker carbon sink function, with
144 values ranging from -206.9 to -17.1 g C m⁻² a⁻¹ whilst shrub lands show even lower carbon sink values,
145 ranging from -89.5 to -40.7 g C m⁻² a⁻¹ [Wei et al., 2021]. Marshes display considerable variability in
146 carbon fluxes, with values ranging from -187 ± 29 g C m⁻² a⁻¹ in Shenzha to -478 g C m⁻² a⁻¹ in Haibei
147 [Qi et al., 2021; Zhao et al., 2005]. Therefore, by synthesizing EC and climate data from multiple sites
148 across the TP, we can clearly understand the spatial and temporal variations of water, heat, CO₂ fluxes
149 and identify the mechanisms that control them.

150 To address these knowledge gaps, this study introduces a comprehensive multi-site observation
151 network for monitoring LA exchanges of water, heat, and CO₂ fluxes across the TP (Figure 1 and Table
152 1). The dataset encompasses 16 stations strategically distributed along major hydrothermal and
153 ecological gradients, including alpine meadow, steppe, shrubland, and forest ecosystems. These
154 standardized, long-term EC observations provide unprecedented spatial coverage, particularly over the
155 data-scarce western and northern TP. The network offers a unique opportunity to investigate (1) What
156 are the characteristics of land-atmosphere water, heat, and CO₂ fluxes across different landscapes of the
157 TP? (2) What are the spatial and temporal distributions of water, heat, and CO₂ fluxes, and what factors
158 influence these variations? This paper introduces the design and implementation of the observation
159 platform, instrument configuration, and standardized data processing methods, followed by an analysis
160 of the spatial-temporal variations of meteorological conditions, energy components, and CO₂ fluxes.
161 Specifically, section 3.1 describes the spatial-temporal patterns of atmospheric meteorological variables
162 such as air temperature, humidity and wind speed. Section 3.2 focuses on liquid precipitation and soil

163 water content, which jointly reflect regional water availability. Section 3.3 examines the energy flux
164 components (sensible and latent heat fluxes, etc.), highlighting differences between wet and dry
165 conditions and section 3.4 analyzes the seasonal variations of carbon fluxes (net ecosystem exchange
166 (*NEE*), gross primary productivity (*GPP*) and ecosystem respiration (*Re*)). By making this dataset
167 publicly available, we aim to fill a critical gap in global flux observations and provide a foundation for
168 advancing land–atmosphere interaction research, model evaluation, and climate prediction over high-
169 elevation ecosystems of the TP.

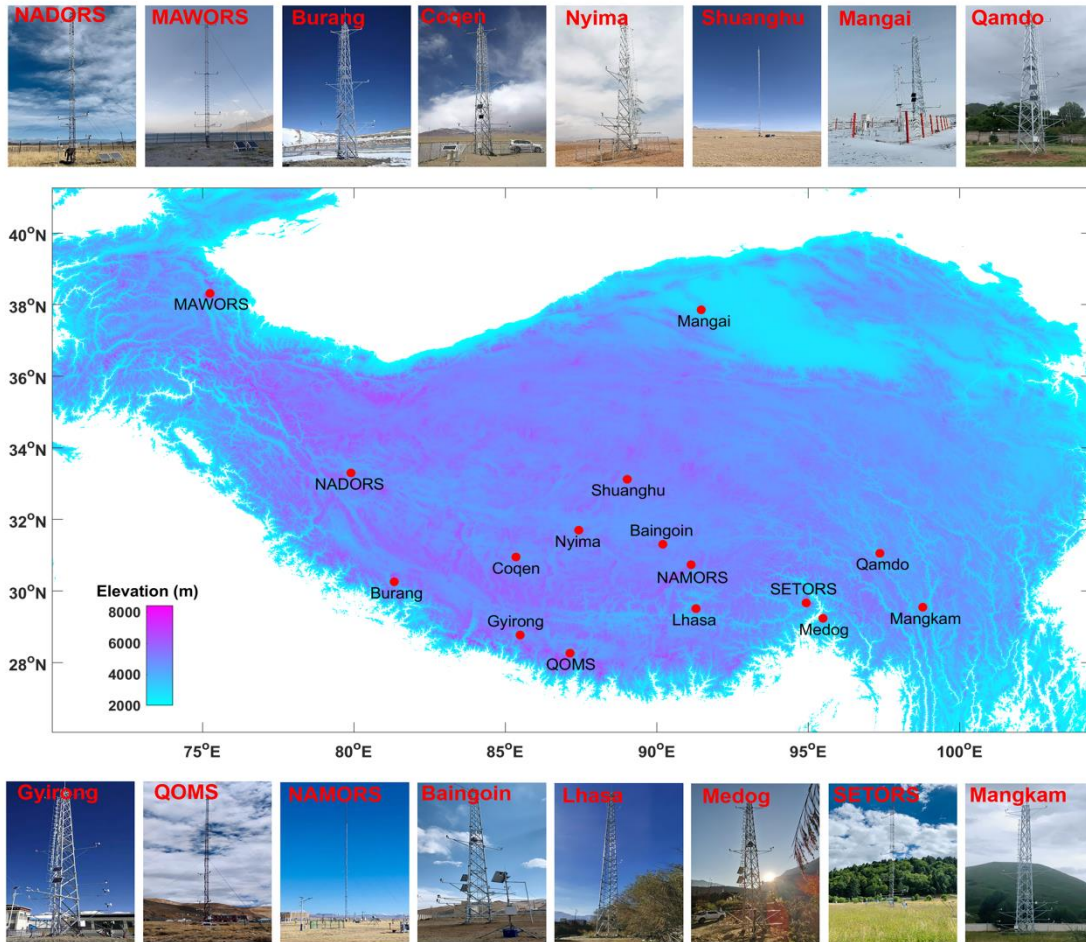
170 **2 The observation platform and methods**

171 **2.1 Introduction of observation platform and instruments configuration**

172 Long-term and quasi-continuous EC networks have been established worldwide across diverse
173 ecosystems, including AmeriFlux and Fluxnet-Canada in North America, EuroFlux and CarboEurope in
174 Europe, AsiaFlux and ChinaFlux in Asia, and OzFlux in Australia [Baldocchi, 2014; Yu et al., 2024].
175 These networks provide critical ground-based measurements for understanding LA energy and material
176 exchanges. Given the TP’s vast area (approximately 2.6 million km²) and extreme environmental
177 conditions — such as high solar radiation, large diurnal temperature variations, and limited
178 precipitation—such EC observations are especially valuable. In this context, the Institute of Tibetan
179 Plateau Research, Chinese Academy of Sciences, established six comprehensive and long-term LA
180 interaction stations in remote and data-scarce regions of TP gradually since 2004 [Ma et al., 2008],
181 including QOMOS (the Qomolangma Atmospheric and Environmental Observation and Research
182 Station, CAS), NAMORS (the Nam Co Monitoring and Research Station for Multisphere Interactions,
183 CAS), SETORS (the Southeast Tibet Observation and Research Station for the Alpine Environment,
184 CAS), NADORS (the Ngari Desert Observation and Research Station, CAS), MAWORS (the Muztagh
185 Ata Westerly Observation and Research Station, CAS), and Shuanghu. Since 2019, the 6 stations were
186 upgraded with new sonic anemometer and gas analyzer sensors gradually (CSAT3 and LI7500DS),
187 enhancing the measurement capabilities. The instrumentation and long-term data at 5 stations covering
188 2006–2021 can be found in Ma et al. [2020] and Ma et al. [2024].

189 Furthermore, the Second Tibetan Plateau Expedition and Research Program (STEP) in 2019 has
190 expanded the network, adding 10 additional LA interaction stations, including Medog, Qamdo, Mangkam,
191 Mangai, Baingoin, Nyima, Jyirong, Burang, Coqen, Lhasa, especially in the remote western and northern
192 regions. The integrated EC devices (IRGASON, Campbell; CSAT3 & LI7500RS in Lhasa), capable of
193 measuring high-frequency (10 Hz) quantities of sonic temperature, water, CO₂, and three-dimensional
194 winds, have been used. This expansion resulted in the creation of the Third Pole Environment Integrated
195 Three-dimensional Observation and Research Platform (TPEITORP, observation platform for short
196 hereafter) for measuring water, heat, and CO₂ fluxes over the TP [Ma et al., 2023]. All stations are
197 equipped with 20 m planetary boundary layer (PBL) towers (40 m at Lhasa) that continuously measure
198 a comprehensive set of meteorological and flux variables. These include air pressure, liquid precipitation,
199 infrared land surface temperature, four-component radiation, soil temperature and moisture at multiple
200 depths, air temperature and humidity at five vertical levels, wind speed and direction at five levels, as
201 well as turbulent fluxes of water, heat, and CO₂. Turbulent fluxes were measured using an EC system
202 installed on each tower, with sensor height and orientation optimized according to prevailing wind
203 directions and local surface roughness conditions. The details of the instrument configuration, station
204 locations, and photographs are provided in Table 1 and Figure 1, respectively. In-situ measurements from

205 these stations, with updated systems, were utilized to analyze the seasonal and diurnal variations of water,
 206 heat, and CO₂ fluxes, as well as the associated energy budget and carbon source–sink dynamics across
 207 contrasting ecosystems and climates. A detailed illustration of the observational environments at 16
 208 stations are as follows.



209
 210 **Figure 1.** The locations and photos of 16 LA interaction stations composing the comprehensive
 211 observation and research platform over the TP. (All the photos have been taken by the authors)

212 QOMOS station is located in Rongbuk Valley, north of Mt. Everest, with a flat observation field
 213 dominated by barren land and sparse vegetation. NAMORS station, on the southeast bank of the third
 214 largest lake (Nam Co) in TP, is covered by alpine meadow. Both QOMOS and NAMORS have in situ
 215 EC and PBL tower systems that have been in operation since 2005, with sensors upgraded in 2019.
 216 SETORS station, located in a mountain valley in the southeast TP, is covered with dense vegetation (50–
 217 60 cm high). The EC and PBL systems were first installed in 2007 and fully upgraded in 2020. NADORS
 218 station, in grassland near Ritu County and Bangong Co, has had an EC system and an automatic weather
 219 station (AWS) since 2008, with a new 20 m PBL tower and a new EC system installed in 2020. MAWORS
 220 station, located near Mustag Mountain and Karakori Lake in Xinjiang, is influenced by westerly winds.
 221 The station has been equipped with an EC system since 2010, and both EC and PBL systems were
 222 updated in October 2020. Shuanghu station, located 3 km north of Shuanghu County, has been
 223 operational since 2012, with a typical alpine grassland surface. The original EC system is still in use,
 224 with new EC and PBL systems added in 2021.

225 Table 1. Overview of instruments configuration and settings at 16 stations, including observation
 226 variables, instrument sensors, observational heights, latitude (lat), longitude (lon), altitude (alt) and
 227 landscape at each station.

Variables	Sensors (Manufacturers)	Heights	Stations (lat, lon, alt, landscape)
Air temperature and humidity	HMP155A-L (Vaisala)	1.5, 2, 4, 10, and 20 m	1. QOMOS (28.36°N, 86.95°E, 4276 m, Alpine desert); 2. NAMORS (30.77°N, 90.98°E, 4730 m, Alpine steppe); 3. SETORS (29.77°N, 94.73°E, 3327 m, Alpine meadow); 4. NADORS (33.39°N, 79.7°E, 4270 m, Alpine desert); 5. MAWORS (38.41°N, 75.05°E, 3668 m, Alpine desert); 6. Shuanghu (33.22°N, 88.83°E, 4947 m, Alpine steppe); 7. Lhasa (40.01 °N, 116.38 °E, 3650 m, City)
Wind speed and direction	05103-L (R.M.Young)	1.5, 2, 4, 10, and 20 m	
Air pressure	CS106 (Vaisala)	-	
Radiations	CNR4 (Kipp & Zonen)	1.5 m	
Precipitation	RG3 (Onset)	-	
Soil temperature and moisture	CS655 (Campbell)	0.1, 0.2, 0.4, 0.8 and 1.6 m	
Soil heat flux	HFP01 (Hukseflux)	0.1 and 0.2 m	
Turbulent flux	CSAT3B (Campbell); LI-7500DS (Li-COR)	Site specific	8. Medog (29.32°N, 95.29°E, 820 m, Forest); 9. Qamdo (31.15°N, 97.17°E, 3307 m, Alpine steppe); 10. Mangkam (29.64°N, 98.59°E, 3840 m, Alpine meadow); 11. Mangai (37.95°N, 91.7°E, 3073 m, Bare ground); 12. Baingoin (31.4°N, 90.01°E, 4709 m, Bare ground); 13. Nyima (31.79°N, 87.23 °E, 4573 m, Alpine steppe); 14. Jyirong (28.86 °N, 85.29°E, 4140 m, Bare ground); 15. Burang (30.35 °N, 81.14°E, 4113 m, Bare ground); 16. Coqen (31.04 °N, 85.16 °E, 4683 m, Alpine steppe);
Air temperature and humidity	HMP155A (Vaisala)	1, 2, 4, 10 and 20 m	
Wind speed and direction	05103 (R.M.Young)	1, 2, 4, 10 and 20 m	
Air pressure	PTB110 (Vaisala)	-	
Radiations	CNR4 (Kipp & Zonen)	1.5 m	
Precipitation	RG3 (Onset)	-	
Soil temperature and moisture	CS655 (Campbell)	0.1, 0.2, 0.4, 0.8, 1.6 m	
Soil heat flux	HFP01 (Hukseflux)	0.1 and 0.4 m	
Turbulent flux	IRGASON (Campbell)	Site specific	
Notes: the heights of turbulent flux measurements from station number 1 to number 16 are 3.0 m, 3.77 m, 3.13 m, 3.7 m, 3 m, 3.2 m, 5 m, 5.5 m, 5.5 m, 3.5 m, 3.5 m, 5.5 m, 3.8 m, 3.5 m, 3.5 m and 40 m respectively. In Lhasa station, the heights of atmosphere variables at 5 layers are 2 m, 4 m, 8 m, 16 m, 32 m.			

228 The stations of Medog, Qamdo, Mangkam, Mangai, Baingoin, Nyima, Jyirong, Burang, Coqen and
 229 Lhasa were gradually established till 2021 with support from STEP program. Medog, Qamdo, and
 230 Mangkam stations are located in the southeastern TP. Medog is located at the southern foot of the eastern
 231 Himalayas, near the Yarlung Zangbo River, with a steep terrain surrounded by subtropical evergreen
 232 broadleaf forest (i.e. banana trees) and crops (i.e., peanuts). Qamdo is situated in the Changdu
 233 Meteorological Bureau's observation field, covered by grass at the top of hilly Changdu City. Mangkam

234 is located at the Mangkang County Meteorological Bureau's external observation field, with a surface
235 covered by 10 cm grass. Mangai station is in the northern part of the TP, with a Gobi desert landscape.
236 The PBL tower and EC system were mounted on the Mangai Meteorological Bureau's external
237 observation field. Baingoin, Nyima, and Coqen stations are located in the west-central TP, each with PBL
238 and EC systems installed at their respective County Meteorological Bureau's observation fields. The land
239 surfaces are bare ground, alpine meadow and alpine meadow, respectively. Jyirong and Burang, located
240 north of the Himalayas, are covered by sparse vegetation and bare land, respectively. Lhasa station,
241 constructed in 2020 and having a 40 m PBL tower, is located in the field observation base of ITPCAS,
242 with roads and low-level buildings surrounded.

243 These stations are distributed across various climatic and environmental regions, covering
244 landscapes such as alpine desert, alpine steppe, alpine meadow, bare ground and city. Some stations,
245 including Mangkam, Baingoin, Qamdo and Lhasa are situated in or adjacent to cities, thus they can be
246 influenced by nearby human activities to some extent. The land surface properties (e.g., land cover,
247 terrain, soil texture) and local climate vary markedly across stations, providing valuable data for
248 generalizing LA interaction schemes across diverse environments and climates over the TP. These
249 differences highlight the complexity of coupled LA interactions, the challenges in obtaining necessary
250 data for model development, and the need for a comprehensive understanding of how land surface
251 processes affect atmospheric conditions and climate predictability. After the construction of the
252 observation platform in 2021, the instruments calibration and maintenance have been carried out twice a
253 year, with field work distance of more than 5000 km and duration of more than 1 month each time. Our
254 efforts to maintain this observation platform aim to bridge the observational gaps in data-scarce regions
255 and to support research on land surface processes, water and energy cycles, and environmental effects
256 across the TP.

257 **2.2 Methods for data processing and analyzing**

258 To study the spatial-temporal variations of meteorological variables and turbulent fluxes of water,
259 heat and CO₂ at these stations and to analyze the influencing factors over the different climatic and
260 environmental conditions, 15 stations have been chosen in this study with an exception of Lhasa, which
261 only captured the measurements during the daytime because of the power malfunction at night. We
262 selected field measurements of more than 2 years, mostly covering the period of May 2021 to July 2023.
263 The proportions of data coverage for meteorological variables and turbulent flux are close to 94% and
264 77%, respectively, with the least data integrity percentage of approximately 50% in Mangai station.
265 Details of data coverage at each station can be found in Table S1 in supplementary material. After
266 accounting for data losses due to instrument failure, power interruptions, and occasional human
267 operational errors, precipitation records from July 2021 to June 2022 were used in this study.
268 Precipitation data gaps occurred at three stations—QOMS (20 %, Feb 1 – Feb 14, May 14 – Jun 1, 2022),
269 NAMORS (22 %, Jan 1 – Mar 21, 2022), and SETORS (6 %, Feb 8 – Feb 12, Mar 27 – Apr 12, 2022)—
270 with the missing periods distributed intermittently throughout the observation year. These data gaps were
271 primarily caused by technical or operational issues. As the rain gauge (RG3, Onset) measures only liquid
272 precipitation during warm seasons and does not record solid precipitation in cold months, the missing
273 data, mostly during winter and pre-monsoon periods, do not affect the conclusions regarding the spatial
274 and temporal variations of liquid precipitation.

275 Currently, meteorological variables were processed following standardized protocols. Abnormal
 276 values—defined as physically implausible measurements such as downward shortwave radiation greater
 277 than 1360 W m^{-2} or less than 0 W m^{-2} , or variables showing unrealistic diurnal or seasonal patterns caused
 278 by sensor or power malfunctions—were flagged and removed after visual inspection and consistency
 279 checks. For turbulent heat flux, two types of open-path EC systems were used across the stations:
 280 CSAT3B and LI-7500DS (stations 1–7) and IRGASON (stations 8–16). These high frequency data were
 281 processed using standard EddyPro software, which includes standard procedures of spike removal,
 282 buoyancy flux conversion to sensible heat, double rotation, as well as ultrasonic virtual temperature
 283 correction and density correction (Webb-Pearman-Leuning correction) [Massman and Lee, 2002;
 284 Mauder and Foken, 2006; Twine et al., 2000]. Quality flags are applied to the flux estimates, considering
 285 steady state test and integral turbulence characteristics test [Mauder et al., 2013]. *NEE* represents the net
 286 vertical CO_2 flux between the ecosystem and the atmosphere and is directly measured by the EC system.
 287 The two main components of the carbon cycle, *GPP* and *Re*, are then estimated from the measured *NEE*
 288 using the standard flux partitioning procedures implemented in the REddyProc package [Wutzler et al.,
 289 2018], where a temperature response function for *NEE* fluxes is used to represent *Re*, with *GPP* derived
 290 as the difference between *Re* and *NEE*. Nighttime *NEE* data with low friction velocity were filtered to
 291 avoid biases, and gaps were filled using the available meteorological data. Specifically, the friction
 292 velocity threshold was estimated using the bootstrapping approach implemented in REddyProc,
 293 following the standard procedure described by Wutzler et al. [2018]. Flux gap-filling was performed
 294 using the marginal distribution sampling method within REddyProc, which estimates missing values
 295 based on relationships with radiation, air temperature, and vapor pressure deficit within a 7-14 day
 296 moving window. Quality control procedures included removing data points affected by sensor
 297 malfunction, spikes, or physically implausible fluxes, and applying the flagging schemes of Mauder et
 298 al. (2013). All low-quality or filtered data were excluded prior to gap-filling and flux partitioning to
 299 ensure data integrity.

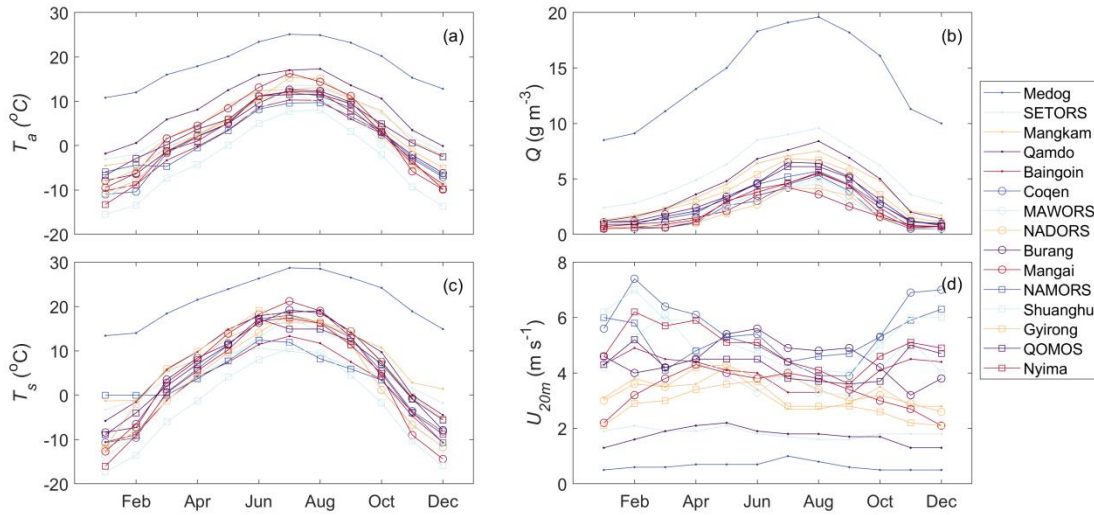
300 Diurnal and seasonal variations of meteorological and turbulent flux variables were analyzed after
 301 filtering out low-quality and spurious data. To reduce the influence of data gaps and enhance
 302 comparability among sites, monthly averaged diurnal cycles of meteorological variables and turbulent
 303 fluxes were used to examine their spatial and temporal patterns across stations. The total annual values
 304 for *ET*, *NEE*, *GPP* and *Re* were obtained by summing the monthly values. During data quality screening,
 305 three stations (QOMOS, NAMORS, and Baingoin) were excluded from the *NEE* flux synthesis because
 306 their *NEE* diurnal cycles exhibited physically inconsistent behavior. Specifically, QOMOS and
 307 NAMORS showed inverted daytime-nighttime variations, while Baingoin displayed abnormally
 308 nighttime CO_2 emissions, probably influenced by nearby biomass burning. Only the remaining 12
 309 stations with reliable CO_2 flux data were retained for spatial and temporal analyses. The energy budget
 310 ratio (*EBR*) and Bowen ratio (*Bo*) at each station were estimated to evaluate energy conditions and energy
 311 consumption. *EBR* ($EBR = \frac{\sum LE + SH}{\sum R_n - G}$) compares the cumulative sum of available energy inputs to the
 312 cumulative sum of turbulent energy outputs over an entire year. Available energy inputs include net
 313 radiation (R_n , W m^{-2}) and ground heat flux (G , W m^{-2}) while turbulent energy outputs include latent heat
 314 flux (LE , W m^{-2}) and sensible heat flux (SH , W m^{-2}). Net radiation can be measured by four components
 315 radiation sensors and is expressed as the difference between downward and upward shortwave ($R_{s\downarrow}$ and
 316 $R_{s\uparrow}$, W m^{-2}) and longwave radiation ($R_{l\downarrow}$ and $R_{l\uparrow}$), specifically: $R_n = R_{s\downarrow} + R_{l\downarrow} - R_{s\uparrow} - R_{l\uparrow}$. Bowen

317 ratio ($Bo = \frac{SH}{LE}$) indicates the relative proportions of energy consumption between SH and LE . Typically,
 318 Bo is high under dry conditions and low under wet conditions.

319 3 Results and discussions

320 3.1 The spatial-temporal variations of atmospheric meteorological variables

321



322

323 **Figure 2.** The seasonal variations of meteorological variables, including (a) air temperature (T_a), (b)
 324 air humidity (Q); (c) land surface temperature (T_s); (d) wind speed at 20 m height (U_{20m}).

325

326 The 15 stations are distributed across diverse environments and climates, resulting in considerable
 327 variations in the seasonal patterns of air temperature (T_a), air humidity (Q), wind speed (U_{20m}) and land
 328 surface temperature (T_s) (Figure 2 and Table 2). The details of seasonal variations of the monthly average
 329 and annual mean of air temperature, wind speed and absolute humidity at the 15 stations can be found in
 330 Table S2-S4. The annual average T_a , T_s , Q and U_{20m} span at ranges of $-3.5\sim 18.5$ °C, $-3.5\sim 21.6$ °C,
 331 $1.88\sim 14.1$ $g\ m^{-3}$ and $0.6\sim 5.6$ $m\ s^{-1}$, respectively. The annual average T_a shows strong positive
 332 correlations (r) with annual average T_s ($r = 0.99, p < 0.01$) and downward long-wave radiation ($R_{L\downarrow}$, $r =$
 333 $0.84, p < 0.01$), and a notable negative correlation with downward short-wave radiation ($R_{S\downarrow}$, $r = -0.72,$
 334 $p < 0.01$) (Figure S1). The high correlation with T_s indicates that strong LA coupling governs the spatial
 335 distribution of T_a , while the negative correlation with $R_{S\downarrow}$ reflects the impact of cloud cover, which
 336 reduces $R_{S\downarrow}$ but increases T_a . Additionally, the annual average T_a exhibits a significant negative
 337 correlation with elevation ($r = -0.92, p < 0.01$). The highest annual average T_a (18.5°C) occurs at Medog
 338 station (820 m a.s.l.), while the lowest (-3.5°C) is observed at Shuanghu station (4947 m a.s.l.). Stations
 339 such as Qamdo (3307 m a.s.l.), SETORS (3327 m a.s.l.), Mangkam (3840 m a.s.l.), and Mangai (3073
 340 m a.s.l.) have annual average values ranging from 5.2°C to 8.6°C , whereas stations above 4000 m have
 341 annual averages from -3.5°C to 3.9°C . Seasonal variations in T_a can also be influenced by climatic and
 342 environmental conditions. For example, despite similar elevations (around 3300 m a.s.l.) and low wind
 343 speeds (approximately $1.8\ m\ s^{-1}$), Qamdo shows larger annual value and amplitude in T_a than that in
 344 SETORS, and it may be attributed to the former's lower moisture condition as well as the strong "urban
 345 heat island" effect. Qamdo, having lower annual precipitation value, is located at a mountaintop grass
 land observation field in the city center, thus, relatively weak evaporated cooling and intense human

346 activities and infrastructure may contribute to Qamdo's elevated T_a . Similarly, in Baingoin and
 347 NAMORS, despite their proximity and similar elevations, NAMORS experiences higher T_a from
 348 October to February and lower temperatures from March to August. Such variations are likely influenced
 349 by the large lake (Nam Co), which has a cooling effect in summer and a warming effect in winter.
 350 Table 2. The annual average meteorological variables, soil water contents (*SM 10cm* and *SM 160cm*
 351 indicate soil moisture at 10 cm and 160 cm, respectively), *NEE*, *GPP*, *Re*, *ET*, *EBR* and *Bo* at 15 stations.

Sites	T_a (°C)	Q (g m^{-3})	U_{20m} (m s^{-1})	T_s (°C)	<i>Prec</i> (mm)	<i>SM</i> <i>10cm</i> (%)	<i>SM</i> <i>160cm</i> (%)	<i>NEE</i> (g C m^2a^{-1})	<i>GPP</i> (g C m^2a^{-1})	<i>Re</i> (g C m^2a^{-1})	<i>ET</i> (mm)	<i>EBR</i> (-)	<i>Bo</i> (-)
Medog	18.5	14.1	0.6	21.6	2164	9 - 25	18 - 43	365	885	1193	571	1.04	0.46
SETORS	5.7	5.64	1.8	6.1	1053	32 - 42	20 - 50	-153	754	633	381	0.634	0.84
Mangkam	5.2	4.07	3.3	6.2	596	4 - 16	20 - 41	-121	454	192	345	0.683	1.09
Qamdo	8.6	4.3	1.7	9.0	456	4 - 14	8 - 19	-133	486	443	354	0.650	0.73
Baingoin	0.5	2.38	4.1	1.2	392	3 - 22	1 - 12	Nan	Nan	Nan	208	0.680	1.52
NAMORS	1.3	2.80	5.2	2.6	304	1 - 9	3 - 6	Nan	Nan	Nan	348	0.828	1.64
Shuanghu	-3.5	2.10	5.3	-3.5	246	1 - 10	9 - 38	-86	165	75	174	0.836	1.88
Gyirong	2.9	3.53	2.8	4.3	237	5 - 14	8 - 20	-58	249	189	218	0.641	2.35
QOMOS	3.9	2.98	4.3	5.6	196	2 - 9	2 - 3	Nan	Nan	Nan	115	0.797	4.11
Nyima	1.3	2.28	4.9	2.3	182	3 - 14	0 - 2	-13	56	36	194	0.631	2.02
Coqen	1.6	2.03	5.6	1.8	137	2 - 6	4 - 9	-15	146	260	155	0.821	3.94
MAWORS	0.8	2.23	4.3	1.0	107	1 - 9	1 - 29	-157	538	368	344	0.623	1.31
NADORS	2.4	1.88	3.5	3.0	64	12 - 48	20 - 50	-174	415	238	222	0.646	0.99
Burang	2.5	3.12	4.5	3.1	58	1 - 4	1 - 5	-65	100	33	121	0.659	4.10
Mangai	3.5	1.93	3.4	4.8	43	1 - 2	1 - 2	-3	69	20	76	0.747	8.32

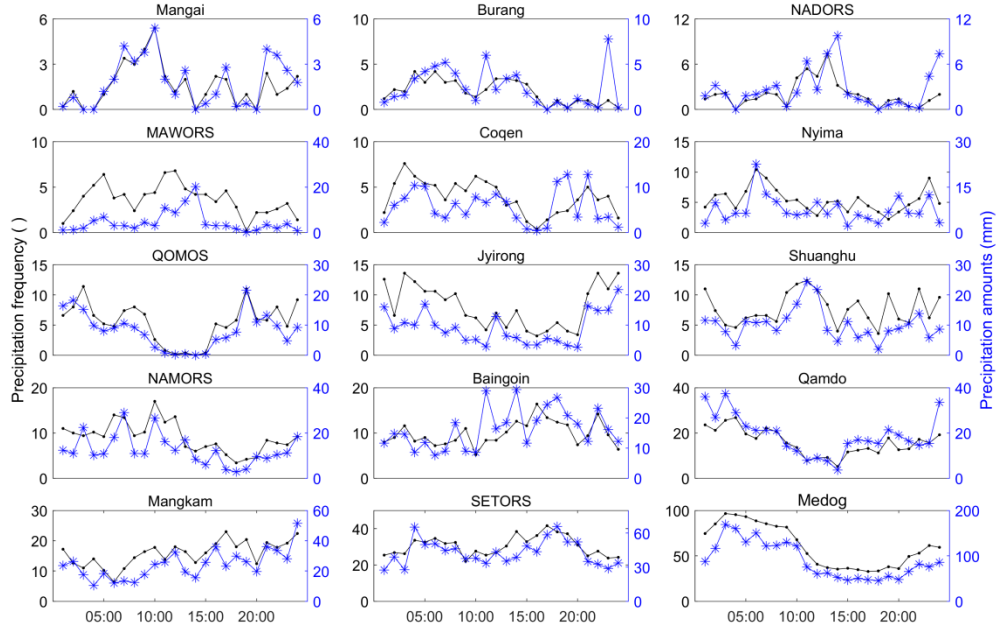
352 Both air humidity (Q) and wind speed at a 20 m height (U_{20m}) at 15 stations show similar
 353 seasonal variations (Figures 2b and 2d). Generally, the seasonal patterns of Q and U_{20m} are
 354 influenced by the interaction of monsoon and westerly systems. Seasonally, the summer monsoon
 355 system leads to the lower values in U_{20m} and higher values in Q , while high values in U_{20m} and low
 356 values in Q during winter are coincident with the dominating westerly system. Spatially, Q decreases
 357 from southeast to northwest across the TP. Medog station, located in a subtropical forest climate,
 358 exhibits the highest annual average Q of 14.1 g m^{-3} . The higher group of annual average Q values
 359 are found at SETORS (5.61 g m^{-3}), Qamdo (4.28 g m^{-3}), and Mangkam (4.12 g m^{-3}), while the rest
 360 of the stations range from 1.74 to 3.67 g m^{-3} . Further, both the annual averages of Q and U_{20m}
 361 correlate with elevation, showing negative and positive correlations of -0.88 ($p < 0.01$) and 0.83
 362 ($p < 0.01$), respectively (Figure S1). U_{20m} is the lowest in Medog, Qamdo, and SETORS, where wind
 363 speeds are generally under 2 m s^{-1} , primarily because of their locations in the southeast mountainous
 364 regions. Conversely, stations at higher elevations with more homogeneous landscapes, such as
 365 Nyima, Coqen, and Shuanghu, experience the highest wind speed.

366 Overall, the 15 stations reveal distinct spatial and seasonal variability in meteorological
 367 conditions across the TP, driven primarily by elevation and large-scale circulation systems. The
 368 combined effects of topography, monsoon and westerly influences, and local factors such as
 369 urbanization and lake regulation shape the observed gradients in temperature, humidity, and wind
 370 speed.

371 3.2 The spatial-temporal variations of liquid precipitation and soil water content

372 The wet-dry condition at each station is mostly correlated with liquid precipitation and soil
373 water content (Table 2). The highest annual precipitation occurs in the southeastern TP, at stations
374 like Medog, SETORS, Mangkam, and Qamdo, where the monsoon system dominates. The monsoon
375 system can bring moist air into the plateau, resulting in annual precipitation values of 2164 mm in
376 Medog, 1053 mm in SETORS, 596 mm in Mangkam, and 456 mm in Qamdo. In contrast, stations
377 with low annual precipitation, such as Mangai, Burang, NADORS, and MAWORS, are located in
378 the western and northern parts of the TP, where mid-latitude westerlies prevail, with annual
379 precipitation below 120 mm. The rest seven stations in the central and western TP, where both
380 westerly and monsoon systems interact, experience annual precipitation ranging from 120 mm to
381 400 mm. Specifically, Baingoin, NAMORS, and Shuanghu, located in the central TP, receive annual
382 precipitation of between 200 mm and 400 mm, while Nyima, Coqen, Gyirong, and QOMOS
383 receive 100 mm to 200 mm per year. This pattern of high in the southeast and low in the northwest
384 aligns with the Global Precipitation Measurement (GPM) product [Li *et al.*, 2021a]. The spatial
385 distribution of soil water content at depths of 10 cm and 160 cm generally mirrors the precipitation
386 pattern, but they can be also influenced by soil properties and local conditions. For example,
387 NADORS, situated near Bangong Co, exhibits the highest soil water content at 10 cm depth. At 160
388 cm depth, stations like Shuanghu, NADORS, MAWORS, and Gyirong show soil water content up
389 to 0.20, indicating pronounced groundwater contribution. In contrast, Mangai, Burang, Coqen, and
390 NAMORS have the lowest soil water contents.

391 Seasonally, liquid precipitation over the TP is primarily concentrated during the summer
392 monsoon seasons, with peaks in July and August (Figure S3), consistent with findings from Yang
393 *et al.* [2023] in central TP. Chen *et al.* [2023] observed that monthly precipitation in the Yarlung
394 Tsangbo Grand Canyon exhibits two peaks, one in April and the other in August, which is also the
395 case for SETORS and Medog. Diurnally, Li *et al.* [2021b] noted that summer precipitation over the
396 TP often occurs in the afternoon and evening. However, the diurnal patterns vary markedly across
397 the 15 stations (Figure 3). Precipitation frequency and amounts followed similar diurnal variations,
398 with notable exceptions at Baingoin and MAWORS, where precipitation frequency peaked between
399 6:00 and 11:00, but the highest rainfall amounts occurred at 14:00. At westerly-dominated stations
400 in the northern TP like Mangai, NADORS, MAWORS, and Shuanghu, precipitation peaks during
401 the day and is minimal at night, though the timing of these peaks varies. In contrast, stations in
402 mountainous regions—Medog, Mangkam, Qamdo, Nyima, and Gyirong—experience peak
403 precipitation mostly at night, similar to findings in Chen *et al.* [2023] for the Yarlung Zangbo Grand
404 Canyon. SETORS, QOMOS, and Coqen exhibit bimodal precipitation patterns, with peaks at night
405 and in the late afternoon. Burang and NAMORS show higher precipitation in the first half of the
406 day, with lower amounts later, and such patterns are probably related with the lake breeze circulation.
407 Generally, daytime rainfall is probably driven by up-slope flows due to surface heating, while the
408 monsoon nocturnal low-level jet may contribute to nighttime rainfall. Further, the local circulations
409 of lake-land breeze and mountain-valley breeze can also modulate the water circulations and impact
410 on the diurnal variation of precipitation.



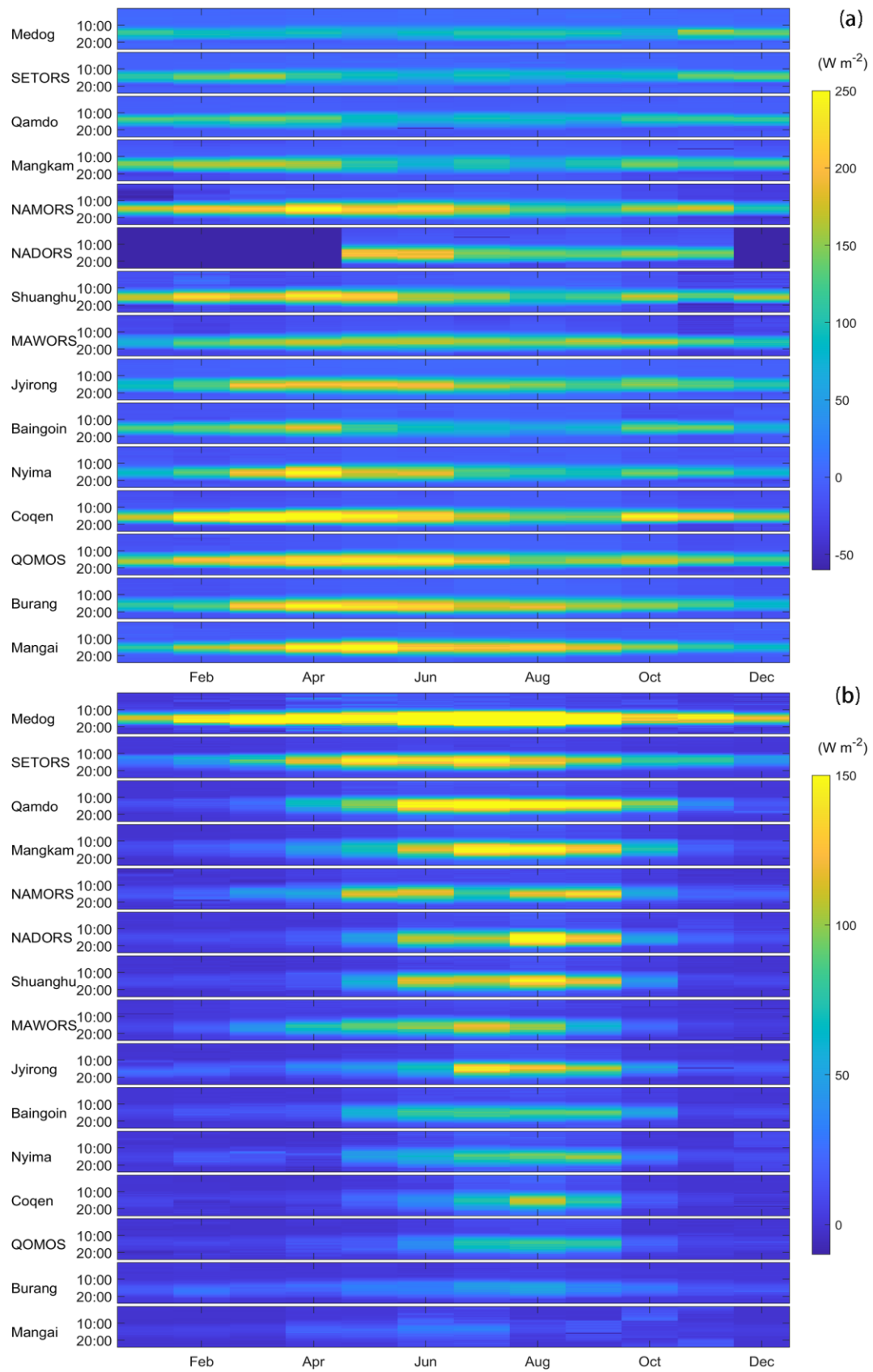
411

412 **Figure 3.** The diurnal variations of liquid precipitation amounts and frequency at 15 stations. Liquid
 413 precipitation frequency indicates the total times of liquid precipitation annually.

414 Overall, precipitation and soil moisture across the TP show a clear southeast–northwest
 415 gradient, decreasing from humid monsoon regions to arid westerly-dominated areas. Seasonal and
 416 diurnal variations reflect the combined influence of the summer monsoon, local topography, and
 417 mesoscale circulations such as mountain–valley and lake–land breezes. These spatial and temporal
 418 patterns highlight strong hydroclimatic heterogeneity and its control on regional LA coupling.

419 **3.3 The spatial-temporal variations of energy flux**

420 Net radiation (R_n) provides the energy source for LA energy and material exchange, and is
 421 mainly divided into three components: ground heat flux (G), SH , and LE . R_n generally shows
 422 positive values in its seasonal variations, indicating that the ground surface acts as a heat source
 423 relative to the overlying atmosphere. R_n peaks in June or July and reaches its lowest in December
 424 or January. SETORS and Gyirong have monthly R_n values of greater than 90 W m^2 , while Baingoin
 425 and Mangai have values of below 70 W m^2 . The other stations show values of between 70 and 90 W
 426 m^2 , which are similar to those reported in previous studies, 4 stations over the TP and 4 stations in
 427 the lower reaches of the Yangtze River region [Yao *et al.*, 2024]. Details for the seasonal variation
 428 of monthly net radiation and monthly ground heat flux and their annual means at the 15 stations can
 429 be found in Table S5-S6. Further, heat storage occurs mainly from March to August, peaking around
 430 June, while heat release is most remarkable from October to February, with the largest release in
 431 December. The annual average of monthly G ranges from -0.01 W m^2 at Qamdo to 2.39 W m^2 at
 432 NADORS. The close-to-zero G values suggest minimal impact of ground heat storage on the energy
 433 budget at an annual scale, while the dominating positive values suggest a warming trend in the
 434 ground, aligning with global warming and the rise in land surface temperature [Duan and Xiao,
 435 2015; Oku *et al.*, 2006; Zhang *et al.*, 2023].



436

437

438

Figure 4. The heat maps for averaged diurnal and seasonal variations of sensible heat flux (a) and latent heat flux (b) at 15 stations.

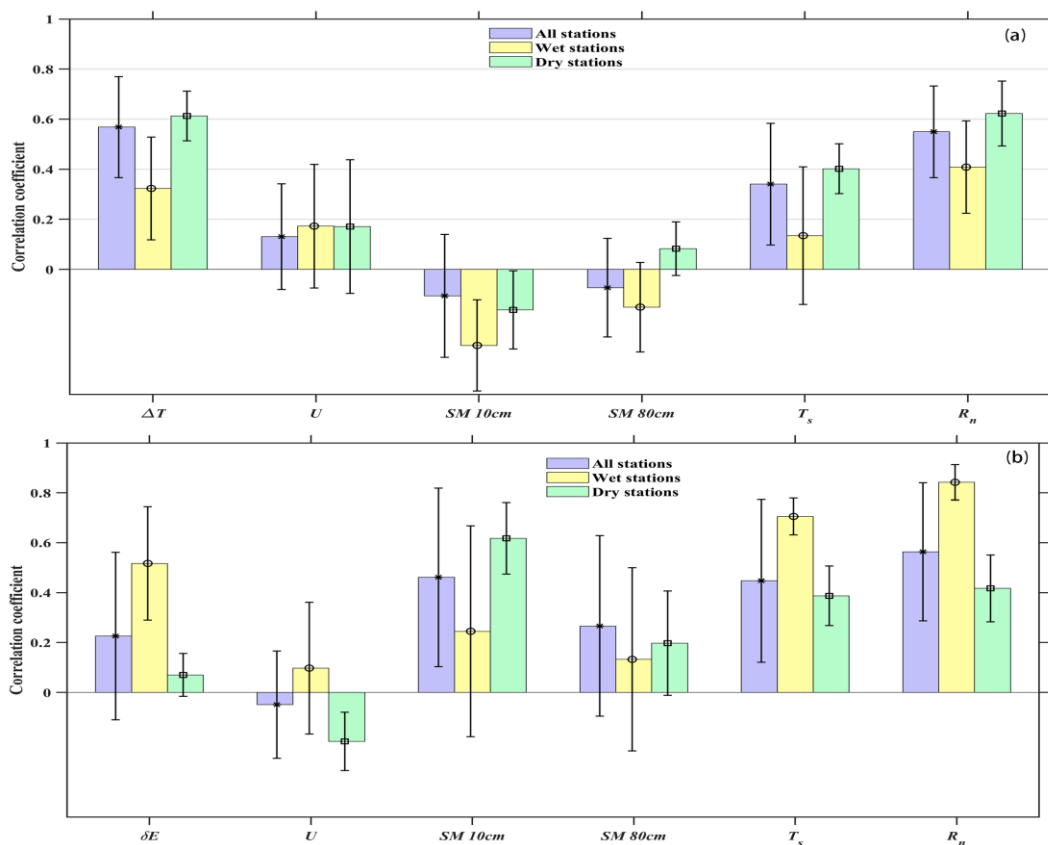
439 Turbulent heat fluxes, including SH and LE , exhibit clear diurnal and seasonal variations
440 (Figure 4), consistent with previous studies on the TP [Ma *et al.*, 2005; Zhong *et al.*, 2019a]. In
441 addition, the seasonal evolution of monthly averaged diurnal SH and LE can be found in Figure S4-
442 S5. SH peaks during the pre-monsoon months of April and May, and is lowest in the cold months
443 of December and January. Stations with sufficient water availability, such as Medog, SETORS,
444 Mangkam, Qamdo, Baingoin, MAWORS, and NADORS, have total annual SH values ranging from
445 269 to 356 $W m^{-2}$. The first five stations receive high precipitation, while the latter two have
446 substantial soil moisture supply. Other stations have total annual SH fluxes exceeding 400 $W m^{-2}$,
447 with QOMOS and Coqen reporting the highest annual values of 582 $W m^{-2}$ and 626 $W m^{-2}$,
448 respectively. LE peaks during the monsoon seasons (July to August) and is not apparent throughout
449 the cold months. Specifically, the total annual LE is only 61.3 $W m^{-2}$ at the extremely dry Mangai
450 station, while Medog records monthly LE values all exceeding 29 $W m^{-2}$. Spatially, LE is showing
451 decreasing pattern from the southeast wet regions to the northwest dry regions. As shown in Table
452 1, the Bo reflects the energy distribution between SH and LE . Medog, SETORS, and Qamdo in the
453 southeast have Bo values of less than 1, indicating dominant heat consumption through the LE , while
454 Mangai, Burang, and QOMOS in the northern and western regions have Bo ratios greater than 4,
455 suggesting the dominant role of SH .

456 The EBR is the ratio of turbulent energy fluxes ($SH + LE$) to available energy ($R_n - G$). The
457 average EBR across the 15 stations is approximately 0.73, ranging from 0.62 to 1.04, with 11 stations
458 between 0.6 and 0.8, while Medog exceeds 1 (Table 2). These values are consistent with results
459 from global eddy flux sites [Wilson *et al.*, 2002]. Imperfect energy balance closure can arise from
460 several factors [Foken, 2008; Mauder *et al.*, 2020], including footprint mismatch, instrumental
461 biases, unaccounted energy storage, flux losses at different frequencies, and neglected advection.
462 The influence of these factors likely varies among sites according to their surface heterogeneity and
463 terrain complexity. A detailed site-level attribution of EBR differences requires further analysis and
464 will be addressed in future work.

465 Following the LA interaction theories, SH (LE) are primarily influenced by land-atmosphere
466 temperature gradients ($\Delta T = T_s - T_a$) or water vapor deficit ($\Delta E = e_s - e_a$, where e_s and e_a are the
467 saturation vapor pressure and the actual vapor pressure respectively), wind speed (U), soil moisture
468 at 10 cm and 80 cm, land surface temperature (T_s) and net radiation (R_n), etc [Wang *et al.*, 2017].
469 The correlation coefficients between SH (LE) and the related variables can be found in Table S7,
470 and the dominating factors for LA turbulent flux are pronouncedly different under dry and wet
471 stations, where energy-related variables are most important in water-sufficient conditions, while
472 water-related variables show dominant role in water-shortage conditions. For example, wet stations
473 such as Medog, SETORS, Mangkam, and Qamdo, which receive substantial precipitation and
474 maintain high soil moisture, exhibit stronger correlations of LE with R_n and T_s than with soil
475 moisture. In contrast, dry stations such as QOMOS, Nyima, Coqen, and Burang, characterized by
476 low precipitation and limited soil moisture, show higher correlations of LE with soil moisture at 10
477 cm than with other variables. Mangai, an extremely dry station with annual precipitation value of
478 only 43.2 mm and very low soil moisture conditions (0.01-0.02), has the smallest annual ET value
479 and no obvious correlations with all the variables. In NADORS, the annual ET has a value of 222.4
480 mm, significantly higher than the annual precipitation amount of 64 mm, and the volumetric water

481 content at 80 cm can reach up to 0.3, suggesting a substantial impact of groundwater supply. Thus,
 482 soil moisture and R_n have comparable high correlation coefficients in NADORS.

483 The correlation coefficients between SH (LE) and related environment variables under
 484 conditions of all stations, wet stations (Medog, SETORS, Mangkam, and Qamdo) and dry stations
 485 (QOMOS, Nyima, Coqen, Burang) are grouped in Figure 5. For all stations included, SH variations
 486 are primarily driven by ΔT , followed by R_n and T_s , with correlation coefficients of 0.57, 0.55 and
 487 0.34, respectively (Figure 5a). Further, SH has a positive correlation with wind speed and a negative
 488 correlation with soil moisture. The correlation coefficients show large diversity under dry and wet
 489 conditions, with generally lower values in wet stations than those in dry stations. For example, the
 490 averaged correlation coefficients between SH and $\Delta T/R_n/T_s$ under dry stations are 0.63/0.65/0.44
 491 while those values (0.32/0.40/0.13) are much smaller under wet conditions. Wind speed has weaker
 492 correlation with SH . but in MAWORS and Medog, the correlation coefficients could approach to
 493 0.5. In NAMORS, there is a negative correlation between wind speed and SH . These phenomenons
 494 may be related with the local circulations of mountain-valley and lake-land breezes, which may lead
 495 to synchronized and opposite variations in such conditions.



496

497 **Figure 5.** The correlation coefficients between sensible heat flux (a), latent heat flux (b) and related
 498 environmental variables at a temporal resolution of hourly under conditions of all stations, wet stations
 499 and dry stations, respectively. The statistical significance of the correlation coefficients for each station
 500 is provided in Table S7.

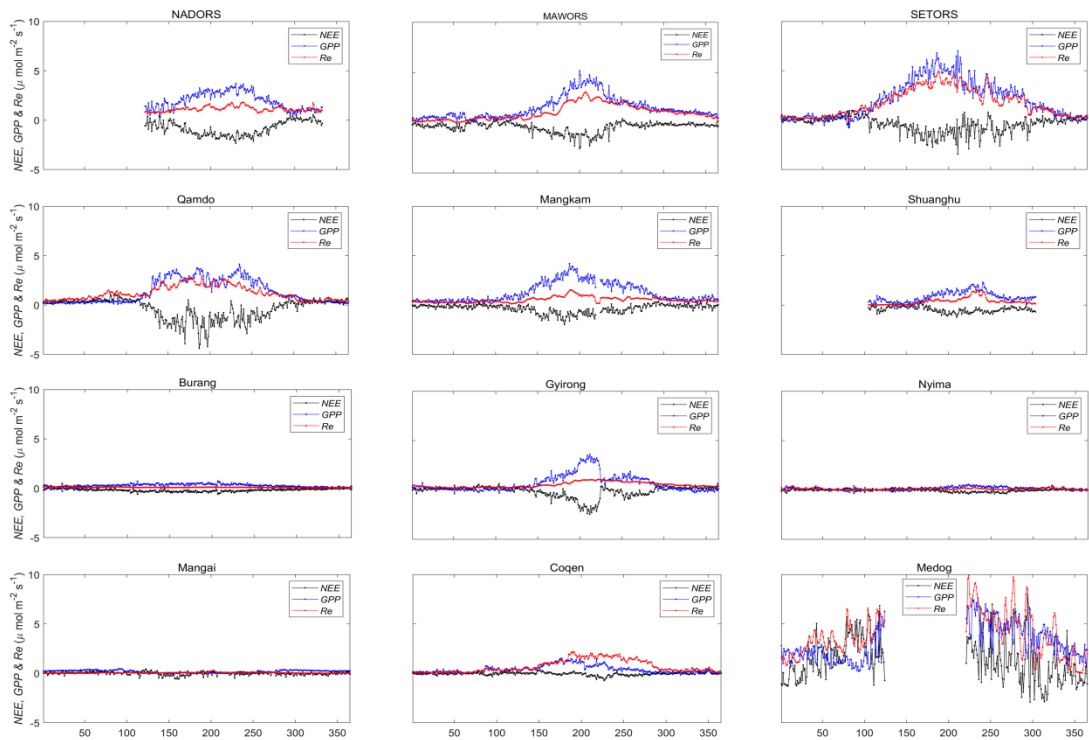
501 The correlations between LE and environmental variables are more complex (Table S7 and
502 Figure 5b). The three paramount factors are R_n , T_s and soil moisture at 10 cm, with correlation
503 coefficients of 0.56, 0.46, 0.45, respectively. For wet stations, the most important variables are
504 energy related variables (R_n and T_s). Stations such as Medog, Mangkam, SETORS, Qamdo,
505 Gyirong, and NADORS follow this pattern, with the first four stations influenced by high
506 precipitation and the latter two by soil water content. ΔE represents the difference between the
507 actual and saturation vapor pressure, indicating the atmospheric moisture deficit. The saturation
508 vapor pressure increases exponentially with temperature—by about 6 – 7% per degree Celsius—so
509 warmer air can hold substantially more water vapor than cooler air. Thus, ΔE shows remarkable
510 high correlations at Medog and SETORS. At stations like Burang, Nyima, MAWORS, and Coqen,
511 the most influential variable is soil moisture, followed by R_n and T_s . Thus, both energy and water
512 availability play dominant roles. At extremely dry station of Mangai, most of the monthly LE values
513 are close to zero, and none of the variations show obvious correlations with LE . For QOMOS, the
514 largest correlation with LE is seen with soil moisture at 10 cm, suggesting that water availability
515 plays a more critical role in ET than energy availability in this region.

516 In a brief summary, turbulent fluxes of SH and LE display clear spatial and seasonal patterns,
517 with the Bowen ratio reflecting this energy partitioning. Correlation analyses reveal that SH is
518 primarily driven by temperature gradients, whereas LE is controlled by energy-related factors in wet
519 regions and by soil moisture availability in dry regions, highlighting the contrasting mechanisms of
520 LA coupling across the TP.

521 **3.4 The seasonal variations of NEE , GPP and Re**

522 The seasonal variations of daily NEE , GPP , and Res averaged over the observational period
523 show remarkable differences across sites, and the sites with relatively good vegetation coverage
524 follow a single-peak distribution pattern, i.e. SETORS, Qamdo, Mangkam, etc., but the other sites,
525 including Burang, Nyima, Coqen, Mangai, show weak or nearly non seasonal variations (Figure 6
526 and Table 2). The carbon absorption and release are determined by vegetation photosynthesis
527 process and ecosystem respiration. The seasonal variation of carbon fluxes follow the vegetation
528 growth, with highest values during the summer peak growing seasons. For example, stations with
529 substantial vegetation growth, such as SETORS, Qamdo, Mangkam, NADORS, and MAWORS,
530 exhibit higher peaks and fluctuations in NEE , GPP , and Re . The first three stations benefit from
531 high precipitation, while the latter two stations receive considerable shallow soil water supply from
532 surrounding lakes or glaciers. These five stations exhibit strong carbon sink capacities, with NEE
533 values all smaller than -120 g C m^{-2} during the growing season. Specifically, NADORS shows the
534 largest NEE value of -174 g C m^{-2} from May to October, while SETORS has the highest daily NEE
535 values, exceeding $6 \text{ g C m}^{-2} \text{ d}^{-1}$. Similarly, GPP and Re values at the 5 stations all exceed 400 g C
536 m^{-2} and 190 g C m^{-2} , with SETORS having the highest GPP and Re values of 754 g C m^{-2} and 633
537 g C m^{-2} , respectively, due to its favorable temperature and water conditions for vegetation growth.
538 In water-limited regions like Mangai and Nyima, carbon fluxes fluctuations are minimal. Daily NEE
539 values remain below $0.5 \text{ g C m}^{-2} \text{ d}^{-1}$, even during the growing season. The total annual NEE values
540 are -3.2 g C m^{-2} and -12.8 g C m^{-2} in Mangai and Nyima, respectively. GPP and Re values are also
541 low, with annual totals below 70 g C m^{-2} for GPP and 40 g C m^{-2} for Re . The smallest annual GPP
542 value is 56 g C m^{-2} at Nyima, and the smallest annual Re value is 20 g C m^{-2} at Mangai. Although

543 annual *NEE* values at SETORS and MAWORS are relatively similar, SETORS has much larger
 544 *GPP* and *Re* values because of the efficient water supply and warm climate. In contrast, [Wang et
 545 al., 2021] reported NADORS with average *GPP* value of 1.60 g C m⁻² d⁻¹ and average *Re* value of
 546 0.71 g C m⁻² d⁻¹ during growing season of 2014-2015, while these values (2.93 g C m⁻² d⁻¹ for *GPP*
 547 and 1.35 g C m⁻² d⁻¹ for *Re*) are much larger during growing season of 2021-2022 in our estimation.
 548 In addition, the maximum net carbon uptake has a value of -2.1 g C m⁻² d⁻¹ in MAWORS during
 549 2015-2016 [Wang et al., 2021], however, the largest *NEE* exchange value is -2.6 g C m⁻² d⁻¹ in our
 550 measurements. Thus, it may indicate the improvement of vegetation status in the two western
 551 stations during the past 10 years [Zhong et al., 2019b].



552
 553 **Figure 6.** The seasonal variations in *NEE*, *GPP*, *Re* across different sites. The negative *NEE* values
 554 indicated a net uptake of CO₂. The black, blue and red lines stand for daily *NEE*, *GPP* and *Re*,
 555 respectively.

556 The annual *NEE* values are negative at 11 out of 12 stations, with exceptions at Medog (Table
 557 1). The annual *NEE* values at the stations of Qamdo, SETORS, Mangkam, MAWORS and
 558 NADORS all smaller than -120 g C, coincident with stations with higher *ET* annual values,
 559 suggesting the significance of water-carbon coupling in land-atmosphere interaction process. At
 560 stations of Shuanghu, Burang, Jyirong, the annual *NEE* values are between -50 g C and -100 g C
 561 and the rest stations of Nyima and Mangai have annual *NEE* values of close to carbon neutral. At
 562 Medog, despite substantial carbon absorption during the daytime, remarkable carbon release at night
 563 caused by soil respiration leads to large carbon release. Mangai, with sparse vegetation, functions
 564 nearly as carbon neutral. An obvious drastic variation of *NEE* values during August at Gyirong
 565 station can be found and it corresponds to a soil drought event caused by water deficit. The water
 566 deficit event results in decrease in *NEE* and *LE* and obvious increase in *T_s* and *SH*. Notably, carbon
 567 absorption primarily occurs during summer growing seasons of May to September and function as
 568 carbon neutral during winter seasons. The spatial distribution of annual *NEE* values generally follow

569 the distribution of water conditions, where sufficient water can promote vegetation growth, allowing
570 photosynthesis to absorb more CO₂ than respiration releases [Wang et al., 2021; Wang et al., 2023].

571 Global forests have been widely recognized as carbon sinks [Hubau et al., 2020; Pan et al.,
572 2024]. Medog station, located in the Yarlung Zangbo River valley, is surrounded by subtropical
573 forests and has an annual *NEE* value of 365 g C, indicating that the land cover acts as an obvious
574 carbon source. Studies have indicated that tropical forests can become carbon sources due to factors
575 such as deforestation, soil respiration exceeding photosynthesis, lingering droughts, and extreme
576 warming [Gatti et al., 2021; Mills et al., 2023; Xie et al., 2016]. During a severe drought in the
577 summer of 2013 in a subtropical forest in China, the ecosystem switched to a net carbon source by
578 late August [Xie et al., 2016]. Mills et al. [2023] reported that tropical forests, following
579 deforestation and degradation, can shift from carbon sinks to carbon sources. Similarly, the Medog
580 station, located in a hot and humid region with complex terrain, has experienced recent site
581 disturbance associated with station construction in the southern area, leading to partial vegetation
582 removal and soil exposure. These disturbances likely enhanced soil and microbial respiration,
583 resulting in net carbon release. Moreover, topographic shading caused by surrounding steep terrain
584 reduces solar radiation exposure, thereby constraining photosynthesis [Wang et al., 2021; Wang et
585 al., 2023]. The pronounced seasonal variation in *GPP* at this site (Figure 6) is mainly driven by
586 monsoonal climatic conditions—*GPP* peaks during the warm and moist summer months when
587 radiation and temperature are favorable but declines markedly during the cooler and cloudier pre-
588 and post-monsoon periods (Figure S6). Although *NEE* values can be obviously negative during the
589 daytime due to photosynthesis, obvious and long-lasting ecosystem respiration at night leads to a
590 net carbon release (Figure S6).

591 Across the TP, carbon fluxes exhibit clear spatial and seasonal variability linked to vegetation
592 cover and water availability. Stations with abundant precipitation or shallow groundwater act as
593 strong carbon sinks, e.g. SETORS, NADORS, while arid sites such as Mangai and Nyima remain
594 nearly carbon neutral. In contrast, the Medog station functions as a carbon source, likely due to
595 vegetation disturbance, soil respiration, and complex topographic and climatic conditions that limit
596 photosynthetic uptake.

597 **4 Summary**

598 The establishment of a comprehensive observation and research platform marks a remarkable
599 advancement in understanding land-atmosphere water, heat and CO₂ flux across diverse stations.
600 The platform features standardized configurations at each station, including an EC system, a 20 m
601 PBL tower measuring wind, temperature, and humidity across five layers, soil moisture and
602 temperature probes at five depths, energy budget probes for radiation components and soil heat flux,
603 a thermal infrared temperature probe, a barometer, and a rain gauge. It covers a range of landscapes
604 such as alpine steppe, alpine meadow, grassland, bare ground, forest, and desert. The observation
605 platform aims to provide long-term, standardized, high-quality data on land-atmosphere interaction
606 processes over the TP, with a particular focus on the data-scarce regions of the western TP. The
607 extensive hydrometeorological dataset offers initial insights into the spatial and temporal variations
608 of meteorological conditions, liquid precipitation, and turbulent fluxes. Diurnal precipitation

609 patterns reveal three types: peak at night, peak during the day, and bimodal peaks. While liquid
610 precipitation can distinguish between water-limited and energy-limited regions, soil moisture—both
611 from surface and deeper layers—also plays a key role in *ET*, as seen in stations like NADORS and
612 Shuanghu. *NEE* fluxes are near zero at bare ground stations, show notable carbon release in forested
613 areas under construction, and function as carbon sinks in most alpine meadows and alpine steppe
614 sites. This platform is critical for supporting scientific research and sustainable development.
615 However, challenges remain in capturing data from remote and heterogeneous regions, as well as
616 limitations in current technologies. Scaling flux towers for global models remains difficult,
617 highlighting the need for robust interpolation and validation techniques. Additionally, further
618 investigation is required to understand the impacts of land-use changes, such as deforestation and
619 reforestation, on turbulent heat fluxes and their feedback to the climate system.

620 **Competing interests**

621 The authors declare that they have no conflict of interests.

622 **Author contribution**

623 BBW and YMM jointly led the writing of this article and were responsible for the establishment
624 and maintenance of the experimental sites and instrumentation. BBW took the lead in dataset
625 consolidation, processed the data into the standardized format described in this study, and drafted
626 the manuscript in collaboration with all co-authors. ZYH, XL, WQM, XLC, CBH, ZPX, YYW,
627 MSL, BM, XDS, WML, and ZLC contributed to the maintenance of the observation systems, data
628 analysis, and provided critical feedback and revisions to the manuscript.

629 **Data availability statement**

630 The hourly dataset including air temperature, air humidity, wind speed, land surface
631 temperature, soil moisture, downward shortwave radiation, downward longwave radiation, upward
632 shortwave radiation, upward longwave radiation, sensible heat flux, latent heat flux, Net ecosystem
633 change can be downloaded freely in the Tibetan Plateau Data Center. The DOI of the dataset is
634 <https://doi.org/10.11888/Atmos.tpdc.302428>. The data can be referenced by Wang and Ma (2025).
635 The web link is <https://data.tpdc.ac.cn/en/disallow/e8032ff8-2437-4363-876f-2af4e4558a4d>. New
636 collected data will be properly processed and added to this web link in the Tibetan Plateau Data
637 Center.

638 **Acknowledgement**

639 This research was jointly funded by the National Key Research and Development Program of
640 China (2023YFF0805300), the National Natural Science Foundation of China (Grant Nos.
641 U2442213 and 42230610), the Youth Innovation Promotion Association of the Chinese Academy
642 of Sciences (Grant No. 2022069), the Second Tibetan Plateau Scientific Expedition and Research
643 Program (Grant No. 2019QZKK0103).

644 **References**

645 André, J.-C., J.-P. Goutorbe, and A. Perrier (1986), HAPEX—MOBILHY: A Hydrologic Atmospheric
646 Experiment the Study of Water Budget and Evaporation Flux at the Climatic Scale, *Bulletin of the*
647 *American Meteorological Society*, 67(2), 138-144, doi:<https://doi.org/10.1175/1520-0477-67.2.138>.

648 Baldocchi, D. (2014), Measuring fluxes of trace gases and energy between ecosystems and the
649 atmosphere – the state and future of the eddy covariance method, *Global Change Biology*, 20(12), 3600-
650 3609, doi:<https://doi.org/10.1111/gcb.12649>.

651 Bei, N., L. Zhao, J. Wu, X. Li, T. Feng, and G. Li (2018), Impacts of sea-land and mountain-valley
652 circulations on the air pollution in Beijing-Tianjin-Hebei (BTH): A case study, *Environmental Pollution*,
653 234, 429-438, doi:<https://doi.org/10.1016/j.envpol.2017.11.066>.

654 Chen, X., D. Cao, Y. Liu, X. Xu, and Y. Ma (2023), An observational view of rainfall characteristics and
655 evaluation of ERA5 diurnal cycle in the Yarlung Tsangbo Grand Canyon, China, *Quarterly Journal of*
656 *the Royal Meteorological Society*, 149(753), 1459-1472, doi:<https://doi.org/10.1002/qj.4468>.

657 Duan, A., and Z. Xiao (2015), Does the climate warming hiatus exist over the Tibetan Plateau?, *Scientific*
658 *Reports*, 5(1), 13711, doi:10.1038/srep13711.

659 Foken, T. (2008), THE ENERGY BALANCE CLOSURE PROBLEM: AN OVERVIEW, *Ecological*
660 *Applications*, 18(6), 1351-1367, doi:<https://doi.org/10.1890/06-0922.1>.

661 Friedlingstein, P., et al. (2022), Global Carbon Budget 2022, *Earth Syst. Sci. Data*, 14(11), 4811-4900,
662 doi:10.5194/essd-14-4811-2022.

663 Gatti, L. V., et al. (2021), Amazonia as a carbon source linked to deforestation and climate change, *Nature*,
664 595(7867), 388-393, doi:10.1038/s41586-021-03629-6.

665 Gentine, P., A. Massmann, B. R. Lintner, S. Hamed Alemohammad, R. Fu, J. K. Green, D. Kennedy, and
666 J. Vilà-Guerau de Arellano (2019), Land–atmosphere interactions in the tropics – a review, *Hydrol. Earth*
667 *Syst. Sci.*, 23(10), 4171-4197, doi:10.5194/hess-23-4171-2019.

668 Gerken, T., T. Biermann, W. Babel, M. Herzog, Y. Ma, T. Foken, and H.-F. Graf (2014), A modelling
669 investigation into lake-breeze development and convection triggering in the Nam Co Lake basin, Tibetan
670 Plateau, *Theoretical and Applied Climatology*, 117(1), 149-167, doi:10.1007/s00704-013-0987-9.

671 Goutorbe, J. P., et al. (1997), An overview of HAPEX-Sahel: a study in climate and desertification,
672 *Journal of Hydrology*, 188-189, 4-17, doi:[https://doi.org/10.1016/S0022-1694\(96\)03308-2](https://doi.org/10.1016/S0022-1694(96)03308-2).

673 Halldin, S., S. E. Gryning, L. Gottschalk, A. Jochum, L. C. Lundin, and A. A. Van de Griend (1999),
674 Energy, water and carbon exchange in a boreal forest landscape — NOPEX experiences, *Agricultural*
675 *and Forest Meteorology*, 98-99, 5-29, doi:[https://doi.org/10.1016/S0168-1923\(99\)00148-3](https://doi.org/10.1016/S0168-1923(99)00148-3).

676 Huang, J., et al. (2023), Global Climate Impacts of Land-Surface and Atmospheric Processes Over the
677 Tibetan Plateau, *Reviews of Geophysics*, 61(3), e2022RG000771,
678 doi:<https://doi.org/10.1029/2022RG000771>.

679 Hubau, W., et al. (2020), Asynchronous carbon sink saturation in African and Amazonian tropical forests,
680 *Nature*, 579(7797), 80-87, doi:10.1038/s41586-020-2035-0.

681 Li, G., Z. Yu, W. Wang, Q. Ju, and X. Chen (2021a), Analysis of the spatial Distribution of precipitation
682 and topography with GPM data in the Tibetan Plateau, *Atmospheric Research*, 247, 105259,
683 doi:<https://doi.org/10.1016/j.atmosres.2020.105259>.

684 Li, L., R. Zhang, P. Wu, M. Wen, and J. Duan (2020), Roles of Tibetan Plateau vortices in the heavy
685 rainfall over southwestern China in early July 2018, *Atmospheric Research*, 245, 105059,
686 doi:<https://doi.org/10.1016/j.atmosres.2020.105059>.

687 Li, P., K. Furtado, T. Zhou, H. Chen, and J. Li (2021b), Convection-permitting modelling improves
688 simulated precipitation over the central and eastern Tibetan Plateau, *Quarterly Journal of the Royal*
689 *Meteorological Society*, 147(734), 341-362, doi:<https://doi.org/10.1002/qj.3921>.

690 Liu, S., et al. (2018), The Heihe Integrated Observatory Network: A Basin-Scale Land Surface Processes
691 Observatory in China, *Vadose Zone Journal*, 17(1), 180072, doi:<https://doi.org/10.2136/vzj2018.04.0072>.

692 Lü, D., Z. Chen, G. Wang, J. Chen, J. Ji, Y. Li, and H. Chen (1997), Inner Mongolia Semi-Arid Grassland
693 Soil-Vegetation-Atmosphere Interaction, *Climatic and Environmental Research*, 2(3), 199-209,
694 doi:10.3878/j.issn.1006-9585.1997.03.01.

695 Ma, N., and Y. Zhang (2022), Increasing Tibetan Plateau terrestrial evapotranspiration primarily driven
696 by precipitation, *Agricultural and Forest Meteorology*, 317, 108887,
697 doi:<https://doi.org/10.1016/j.agrformet.2022.108887>.

698 Ma, Y., S. Fan, H. Ishikawa, O. Tsukamoto, T. Yao, T. Koike, H. Zuo, Z. Hu, and Z. Su (2005), Diurnal
699 and inter-monthly variation of land surface heat fluxes over the central Tibetan Plateau area, *Theoretical*
700 *and Applied Climatology*, 80(2), 259-273, doi:10.1007/s00704-004-0104-1.

701 Ma, Y., et al. (2020), A long-term (2005–2016) dataset of hourly integrated land–atmosphere interaction
702 observations on the Tibetan Plateau, *Earth Syst. Sci. Data*, 12(4), 2937-2957, doi:10.5194/essd-12-2937-
703 2020.

704 Ma, Y., Y. Wang, and C. Han (2018), Regionalization of land surface heat fluxes over the heterogeneous
705 landscape: from the Tibetan Plateau to the Third Pole region, *International Journal of Remote Sensing*,
706 39(18), 5872-5890, doi:10.1080/01431161.2018.1508923.

707 Ma, Y., et al. (2024), Dataset of spatially extensive long-term quality-assured land–atmosphere
708 interactions over the Tibetan Plateau, *Earth Syst. Sci. Data*, 16(6), 3017-3043, doi:10.5194/essd-16-
709 3017-2024.

710 Ma, Y., et al. (2023), Comprehensive study of energy and water exchange over the Tibetan Plateau: A
711 review and perspective: From GAME/Tibet and CAMP/Tibet to TORP, TPEORP, and TPEITORP, *Earth-*
712 *Science Reviews*, 237, 104312, doi:<https://doi.org/10.1016/j.earscirev.2023.104312>.

713 Ma, Y. M., S. C. Kang, L. P. Zhu, B. Q. Xu, L. D. Tian, and T. D. Yao (2008), TIBETAN OBSERVATION
714 AND RESEARCH PLATFORM Atmosphere-Land Interaction over a Heterogeneous Landscape,
715 *Bull.amer.meteor.soc*, 89(10), 1487-1492.

716 Massman, W. J., and X. Lee (2002), Eddy covariance flux corrections and uncertainties in long-term
717 studies of carbon and energy exchanges, *Agricultural and Forest Meteorology*, 113(1), 121-144,
718 doi:[https://doi.org/10.1016/S0168-1923\(02\)00105-3](https://doi.org/10.1016/S0168-1923(02)00105-3).

719 Mauder, M., M. Cuntz, C. Drüe, A. Graf, C. Rebmann, H. P. Schmid, M. Schmidt, and R. Steinbrecher
720 (2013), A strategy for quality and uncertainty assessment of long-term eddy-covariance measurements,
721 *Agricultural and Forest Meteorology*, 169, 122-135, doi:<https://doi.org/10.1016/j.agrformet.2012.09.006>.

722 Mauder, M., and T. Foken (2006), Impact of post-field data processing on eddy covariance flux estimates
723 and energy balance closure, *Meteorologische Zeitschrift*, 15(6), 597-609.

724 Mauder, M., T. Foken, and J. Cuxart (2020), Surface-Energy-Balance Closure over Land: A Review,
725 *Boundary-Layer Meteorology*, 177(2), 395-426, doi:10.1007/s10546-020-00529-6.

726 Mills, M. B., et al. (2023), Tropical forests post-logging are a persistent net carbon source to the
727 atmosphere, *Proceedings of the National Academy of Sciences*, 120(3), e2214462120,
728 doi:doi:10.1073/pnas.2214462120.

729 Oku, Y., H. Ishikawa, S. Haginoya, and Y. Ma (2006), Recent Trends in Land Surface Temperature on
730 the Tibetan Plateau, *Journal of Climate*, 19(12), 2995-3003, doi:<https://doi.org/10.1175/JCLI3811.1>.

731 Pan, Y., Birdsey, R.A., Phillips, O.L. et al. The enduring world forest carbon sink. *Nature* 631, 563–569
732 (2024)

733 Qi, Y., D. Wei, H. Zhao, and X. Wang (2021), Carbon Sink of a Very High Marshland on the Tibetan
734 Plateau, *Journal of Geophysical Research: Biogeosciences*, 126(4), e2020JG006235,
735 doi:<https://doi.org/10.1029/2020JG006235>.

736 Santanello, J. A., et al. (2018), Land–Atmosphere Interactions: The LoCo Perspective, *Bulletin of the*
737 *American Meteorological Society*, 99(6), 1253-1272, doi:<https://doi.org/10.1175/BAMS-D-17-0001.1>.

738 Sellers, P., et al. (1995), The Boreal Ecosystem–Atmosphere Study (BOREAS): An Overview and Early
739 Results from the 1994 Field Year, *Bulletin of the American Meteorological Society*, 76(9), 1549-1577,
740 doi:[https://doi.org/10.1175/1520-0477\(1995\)076<1549:TBESAO>2.0.CO;2](https://doi.org/10.1175/1520-0477(1995)076<1549:TBESAO>2.0.CO;2).

741 Sellers, P. J., F. G. Hall, G. Asrar, D. E. Strelbel, and R. E. Murphy (1992), An overview of the First
742 International Satellite Land Surface Climatology Project (ISLSCP) Field Experiment (FIFE), *Journal of*
743 *Geophysical Research: Atmospheres*, 97(D17), 18345-18371, doi:<https://doi.org/10.1029/92JD02111>.

744 Seo, Y.-W., and K.-J. Ha (2022), Changes in land-atmosphere coupling increase compound drought and
745 heatwaves over northern East Asia, *npj Climate and Atmospheric Science*, 5(1), 100,
746 doi:10.1038/s41612-022-00325-8.

747 Suni, T., et al. (2015), The significance of land-atmosphere interactions in the Earth system—iLEAPS
748 achievements and perspectives, *Anthropocene*, 12, 69-84,
749 doi:<https://doi.org/10.1016/j.ancene.2015.12.001>.

750 Turetsky, M. R., et al. (2020), Carbon release through abrupt permafrost thaw, *Nature Geoscience*, 13(2),
751 138-143, doi:10.1038/s41561-019-0526-0.

752 Twine, T. E., W. P. Kustas, J. M. Norman, D. R. Cook, P. R. Houser, T. P. Meyers, J. H. Prueger, P. J.
753 Starks, and M. L. Wesely (2000), Correcting eddy-covariance flux underestimates over a grassland,
754 *Agricultural and Forest Meteorology*, 103(3), 279-300, doi:[https://doi.org/10.1016/S0168-](https://doi.org/10.1016/S0168-1923(00)00123-4)
755 [1923\(00\)00123-4](https://doi.org/10.1016/S0168-1923(00)00123-4).

756 Wang, Shuzhou, and Yaoming (2011), Characteristics of Land-Atmosphere Interaction Parameters over
757 the Tibetan Plateau, *Journal of Hydrometeorology*.

758 Wang, B., Y. Ma, W. Ma, and Z. Su (2017), Physical controls on half-hourly, daily, and monthly turbulent
759 flux and energy budget over a high-altitude small lake on the Tibetan Plateau, *Journal of Geophysical*
760 *Research: Atmospheres*, 122(4), 2289-2303, doi:<https://doi.org/10.1002/2016JD026109>.

761 Wang, B., Ma, Y. (2025). Meteorological variables and eddy fluxes at 15 land-atmosphere interaction
762 stations over the Tibetan Plateau (May-2021 to July 2023). National Tibetan Plateau / Third Pole
763 Environment Data Center. <https://doi.org/10.11888/Atmos.tpdc.302428>.

764 Wang, Y., J. Xiao, Y. Ma, J. Ding, X. Chen, Z. Ding, and Y. Luo (2023), Persistent and enhanced carbon
765 sequestration capacity of alpine grasslands on Earth’s Third Pole, *Science Advances*, 9.

766 Wang, Y., J. Xiao, Y. Ma, Y. Luo, Z. Hu, F. Li, Y. Li, L. Gu, Z. Li, and L. Yuan (2021), Carbon fluxes and
767 environmental controls across different alpine grassland types on the Tibetan Plateau, *Agricultural and*
768 *Forest Meteorology*, 311, 108694, doi:<https://doi.org/10.1016/j.agrformet.2021.108694>.

769 Wei, D., Y. Qi, Y. Ma, X. Wang, W. Ma, T. Gao, L. Huang, H. Zhao, J. Zhang, and X. Wang (2021), Plant
770 uptake of CO₂ outpaces losses from permafrost and plant respiration on the Tibetan Plateau,
771 *Proceedings of the National Academy of Sciences*, 118(33), e2015283118,
772 doi:10.1073/pnas.2015283118.

773 Wilson, K., et al. (2002), Energy balance closure at FLUXNET sites, *Agricultural and Forest*
774 *Meteorology*, 113(1), 223-243, doi:[https://doi.org/10.1016/S0168-1923\(02\)00109-0](https://doi.org/10.1016/S0168-1923(02)00109-0).

775 Wu, G., and Y. Zhang (1998), Tibetan Plateau Forcing and the Timing of the Monsoon Onset over South
776 Asia and the South China Sea, *Monthly Weather Review*, 126(4), 913-927.

777 Wu, G., et al. (2023), An Integrated Research Plan for the Tibetan Plateau Land–Air Coupled System
778 and Its Impacts on the Global Climate, *Bulletin of the American Meteorological Society*, 104(1), E158-
779 E177, doi:<https://doi.org/10.1175/BAMS-D-21-0293.1>.

780 Wutzler, T., A. Lucas-Moffat, M. Migliavacca, J. Knauer, K. Sickel, L. Šigut, O. Menzer, and M.
781 Reichstein (2018), Basic and extensible post-processing of eddy covariance flux data with REddyProc,
782 *Biogeosciences*, 15(16), 5015-5030, doi:10.5194/bg-15-5015-2018.

783 Xie, Z., L. Wang, B. Jia, and X. Yuan (2016), Measuring and modeling the impact of a severe drought
784 on terrestrial ecosystem CO₂ and water fluxes in a subtropical forest, *Journal of Geophysical Research:*
785 *Biogeosciences*, 121(10), 2576-2587, doi:<https://doi.org/10.1002/2016JG003437>.

786 Xu, X., and L. Chen (2006), Advances of the Study on Tibetan Plateau Experiment of Atmospheric
787 Sciences, *Journal of Applied Meteorological Science*, 17(6), 756-772.

788 Yang, K., et al. (2023), Cross-sectional rainfall observation on the central-western Tibetan Plateau in the
789 warm season: System design and preliminary results, *Science China Earth Sciences*, 66(5), 1015-1030,
790 doi:10.1007/s11430-022-1081-4.

791 Yang, K., T. Koike, H. Ishikawa, O. Kim, X. Li, H. Liu, S. Liu, M. A. Yaoming, and J. Wang (2008),
792 Turbulent Flux Transfer over Bare-Soil Surfaces; Characteristics and Parameterization, *Journal of*
793 *Applied Meteorology and Climatology*(1), 47.

794 Yao, N., Y. Ma, B. Wang, J. Zou, J. Sun, and Z. Xie (2024), A comparative study of the land–atmosphere
795 energy and water exchanges over the Tibetan Plateau and the Yangtze River Region, *Atmospheric and*
796 *Oceanic Science Letters*, 17(2), 100447, doi:<https://doi.org/10.1016/j.aosl.2023.100447>.

797 Ye, D.-Z., and G.-X. Wu (1998), The role of the heat source of the Tibetan Plateau in the general
798 circulation, *Meteorology and Atmospheric Physics*, 67(1), 181-198, doi:10.1007/BF01277509.

799 Yu, G.-R., Z. Chen, and Y.-P. Wang (2024), Carbon, water and energy fluxes of terrestrial ecosystems in
800 China, *Agricultural and Forest Meteorology*, 346, 109890,
801 doi:<https://doi.org/10.1016/j.agrformet.2024.109890>.

802 Yuan, L., X. Chen, Y. Ma, C. Han, B. Wang, and W. Ma (2024), Long-term monthly 0.05° terrestrial
803 evapotranspiration dataset (1982–2018) for the Tibetan Plateau, *Earth Syst. Sci. Data*, 16(2), 775-801,
804 doi:10.5194/essd-16-775-2024.

805 Yuan, L., Y. Ma, X. Chen, Y. Wang, and Z. li (2021), An Enhanced MOD16 Evapotranspiration Model
806 for the Tibetan Plateau During the Unfrozen Season, *Journal of Geophysical Research: Atmospheres*,
807 126, doi:10.1029/2020JD032787.

808 Zhang, C., D.-H. Qin, and P.-M. Zhai (2023), Amplification of warming on the Tibetan Plateau, *Advances*
809 *in Climate Change Research*, 14(4), 493-501, doi:<https://doi.org/10.1016/j.accre.2023.07.004>.

810 Zhang, Y., N. Wagner, K. Goergen, and S. Kollet (2024), Summer evapotranspiration–cloud feedbacks in
811 land–atmosphere interactions over Europe, *Climate Dynamics*, doi:10.1007/s00382-024-07475-w.

812 Zhao, L., Y. Li, X. Zhao, S. Xu, Y. Tang, G. Yu, S. Gu, M. Du, and Q. Wang (2005), Comparative study
813 of the net exchange of CO₂ in 3 types of vegetation ecosystems on the Qinghai-Tibetan Plateau, *Chinese*
814 *Science Bulletin*, 50(16), 1767-1774, doi:10.1360/04wd0316.

815 Zhong, L., Y. Ma, Z. Hu, Y. Fu, Y. Hu, X. Wang, M. Cheng, and N. Ge (2019), Estimation of hourly land
816 surface heat fluxes over the Tibetan Plateau by the combined use of geostationary and polar-orbiting
817 satellites, *Atmos. Chem. Phys.*, 19(8), 5529-5541, doi:10.5194/acp-19-5529-2019.

818 Zhu, L., Z. Meng, F. Zhang, and P. M. Markowski (2017), The influence of sea- and land-breeze
819 circulations on the diurnal variability in precipitation over a tropical island, *Atmos. Chem. Phys.*, *17*(21),
820 13213-13232, doi:10.5194/acp-17-13213-2017.
821